

Low-energy spin excitations in field-induced phases of the spin-ladder antiferromagnet BiCu_2PO_6

Patrick Pilch,¹ Kirill Amelin,² Gary Schmiedinghoff,³ Anneke Reinold,¹ Changqing Zhu,¹
Kirill Yu. Povarov,⁴ Sergei Zvyagin,⁴ Hans Engelkamp,⁵ Yin-Ping Lan,⁶ Guo-Jiun Shu,⁶ F. C. Chou,⁷
Urmaz Nagel,² Toomas Rõõm,² Götz S. Uhrig,¹ Benedikt Fauseweh,^{1,3,*} and Zhe Wang^{1,†}

¹*Department of Physics, TU Dortmund University, 44227 Dortmund, Germany*

²*National Institute of Chemical Physics and Biophysics, 12618 Tallinn, Estonia*

³*Institute of Software Technology, German Aerospace Center (DLR), 51147 Cologne, Germany*

⁴*Dresden High Magnetic Field Laboratory (HLD-EMFL) and Würzburg-Dresden Cluster of Excellence ct.qmat, Helmholtz-Zentrum Dresden-Rossendorf (HZDR), 01328 Dresden, Germany*

⁵*High Field Magnet Laboratory (HFML-EMFL), Radboud University, Toernooiveld 7, 6525 ED Nijmegen, The Netherlands*

⁶*Department of Materials & Mineral Resources Engineering, Institute of Mineral Resources Engineering, National Taipei University of Technology, Taipei 10608, Taiwan*

⁷*Center for Condensed Matter Sciences, National Taiwan University, Taipei 10617, Taiwan*

(Dated: October 1, 2024)

We report on terahertz spectroscopic measurements of quantum spin dynamics on single crystals of a spin-1/2 frustrated spin-ladder antiferromagnet BiCu_2PO_6 as a function of temperature, polarization, and applied external magnetic fields. Spin triplon excitations are observed at zero field and split in applied magnetic fields. For magnetic fields applied along the crystallographic a axis, a quantum phase transition at $B_{c1} = 21.4$ T is featured by a low-energy excitation mode emerging above B_{c1} which indicates a gap reopening. For fields along the b axis and the c axis, different field dependencies are observed for the spin triplon excitations, whereas no low-lying modes could be resolved at field-induced phase transitions. We perform a theoretical analysis of the magnetic field dependence of the spin triplon modes by using continuous unitary transformations to determine an effective low energy Hamiltonian. Through an exhaustive parameter search we find numerically optimized parameters to very well describe the experimentally observed modes, which corroborate the importance of significant magnetic anisotropy in the system.

I. INTRODUCTION

Low-dimensional quantum magnets are a captivating material class in condensed matter physics due to their manifestation of quantum fluctuations and/or unconventional ordered spin states due to enhanced quantum effects. Quantum spin-dimerized antiferromagnets feature a spin-singlet ground state which is separated from gapped $S = 1$ spin-triplet excitations - the so-called triplons [1, 2]. In a basic scenario, the application of a magnetic field B leads to the splitting of the triplon modes. The low-lying triplon branch softens until the gap closes at a critical field B_c where the Zeeman energy equals the spin gap value at zero field, leading to a field-induced quantum phase transition. Depending on the interplay between the repulsive boson interaction arising from the hardcore nature of triplons and the gain in kinetic energy from the Zeeman energy, the field-induced phases can exhibit exotic properties, such as magnon Bose-Einstein condensation (BEC) indicated by staggered magnetization [3, 4], or supersolid states close to fractional magnetization plateaus (see e.g. [5–7]).

In spin-1/2 antiferromagnets, a singlet-triplet gap can arise in even-legged spin ladders [8], spin dimerized systems [9, 10], or spin chains with alternating exchange interactions [11] or frustrated next-nearest neighbor couplings [12, 13], or exchange isotropy [14, 15]. BiCu_2PO_6 (BCPO), a frustrated

two-leg spin ladder with alternating next-nearest-neighbor interactions, is therefore a compelling system for the investigation of magnetic ordering phenomena and quantum phase transitions driven by frustration and quantum fluctuations [16]. The magnetic structure of BiCu_2PO_6 is presented in Fig. 1 [16–20], where the exchange interactions between Cu^{2+} $S = 1/2$ spins with two inequivalent crystallographic sites are indicated by different bond colors. Spin ladders are running in the bc plane along the b axis with the intra-rung exchange interaction denoted by J . Along the ladder both nearest- and next-nearest neighbor exchanges [see Fig. 1(c)] are important for understanding the magnetic properties. Inter-ladder coupling in the a direction is smaller by about one order of magnitude. Dzyaloshinskii-Moriya (DM) interactions are allowed and considerable for certain bonds. Previous experimental studies of BiCu_2PO_6 revealed numerous interesting physical phenomena, e.g., a phonon coupling to the spin lattice [21], a strong dependence of the ground state on the pressure during crystal growth [17], and a strong phonon contribution to the thermal conductivity alongside a universal spin thermal conductivity contribution [22]. The magnetic properties of BiCu_2PO_6 have been studied by measuring magnetization [16, 23], magnetic susceptibility [19, 24], heat capacity [19, 25], Raman scattering [26], and Knight shift [27, 28]. Inelastic neutron scattering (INS) experiments [29, 30] have unveiled spin excitations with an incommensurate wave vector in a quantum-disordered low temperature phase. Together with theoretical investigations using quadratic bond-operator theory [29] and exact diagonalization [16] these results emphasize the importance of multi-triplon excitations, corroborated by Raman scattering experiments [26]. However, the

* benedikt.fauseweh@tu-dortmund.de

† zhe.wang@tu-dortmund.de

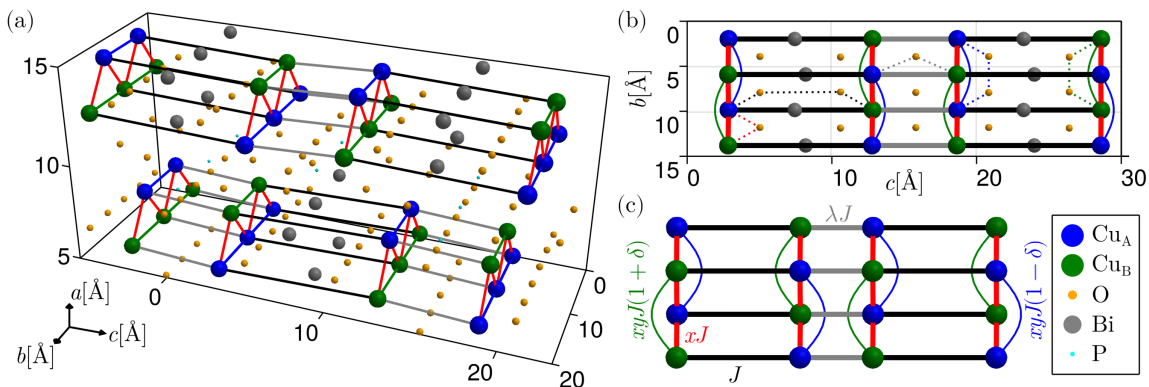


Figure 1. Structure for BCPO with colored lines to indicate interactions. The (a) three-dimensional view reveals two-dimensional bilayers of interactions, the latter of which are depicted by straight lines. Panel (b) shows a single bilayer from above, where the dotted lines indicate the oxygen atoms involved in each (super-)exchange interaction. The final, abstracted spin model including the names of the interactions is depicted in (c). Each interacting pair on the same ladder is also subjected to the SAE and DM interactions.

observed dispersion relation of the magnetic excitations, including the bending of the low-energy branch near the magnetic excitation continuum in the reciprocal space, have not been fully understood despite numerous theoretical attempts [29, 31–33], which calls for further experimental studies.

A nuclear magnetic resonance (NMR) study in external magnetic fields along the b axis revealed deviations from a standard BEC due to an unusual critical exponent, highlighting the significance of anisotropic Dzyaloshinskii-Moriya and the symmetric anisotropic exchange (SAE) interactions [34], which is consistent with the findings of previous magnetization measurements [16]. A field-induced intermediate phase with an incommensurate spiral structure [35] was suggested, which was described theoretically by the formation of a soliton lattice, i.e. fractionalized spin-1/2 quantum domain walls [34, 36]. In higher fields, the system undergoes a second incommensurate-commensurate (IC-C) phase transition. For fields along the a or c axis, a comprehensive NMR study has not been performed [34], but specific heat measurements did not support the formation of a soliton lattice [37], where magnetic anisotropy in the g tensor or in the Dzyaloshinskii-Moriya interactions could be more influential and bring more complexity to the theoretical analysis [34].

In this work we focus on the study of magnetic excitations in BiCu₂PO₆ by performing high-resolution terahertz (THz) spectroscopy and electron spin resonance (ESR) spectroscopy as a function of temperature and applied high magnetic fields. The dependence of the magnetic excitations on the applied magnetic field along different crystallographic directions is obtained and quantitatively compared to our theoretical analysis. In particular, we provide spin dynamic evidence on field-induced quantum phase transition and determine the underlying spin interaction Hamiltonian.

II. EXPERIMENTAL DETAILS

Single crystals of BiCu₂PO₆ were grown by floating-zone method [26]. We prepared two sample orientations: a wedged

a -cut sample measuring $5 \times 5 \text{ mm}^2$ with an average thickness of 1 mm and a b -cut sample of the same dimensions but with a thickness of 1.1 mm. Zero-field polarized THz transmission spectra were acquired using the TeslaFIR spectrometer in a magneto-optical cryostat [38], and differential absorption $\Delta\alpha(T) = \alpha(T) - \alpha(30 \text{ K})$ was calculated using the $T = 30 \text{ K}$ spectrum as a reference. Similarly, polarized low-field THz spectroscopy experiments ($B \leq 16 \text{ T}$) were conducted with magnetic fields applied using a superconducting magnet in Faraday and Voigt geometry. As a reference, the 0 T spectrum was used to calculate the differential absorption $\Delta\alpha(B) = \alpha(B) - \alpha(0 \text{ T})$. $\alpha(0 \text{ T})$ was recovered from a median of all measured $\Delta\alpha(B)$. This method allows to extract the magnetic-field dependent part of the absorption coefficient. Unpolarized high-field ESR experiments were performed at the Dresden High Magnetic Field Laboratory (Hochfeld Magnetlabor-Dresden), using a multi-frequency ESR spectrometer (similar to that described in Ref. [39]), in magnetic fields up to 60 T. We used VDI microwave-chain radiation sources (product of Virginia Diodes, Inc., USA) to generate radiation in the sub-THz frequency range. A hot-electron n-InSb bolometer (product of QMC Instruments Ltd., UK), operated at 4.2 K, was used as a radiation detector. Additional unpolarized high-field spectroscopy measurements with magnetic fields up to 28 T and at a temperature of 1.4 K were performed at the Nijmegen High Field Magnet Laboratory (HFML), using a Bruker IFS 113v Fourier-transform spectrometer. The corresponding differential absorption spectra were obtained by subtracting the average of the absorption spectra of all magnetic fields.

III. EXPERIMENTAL RESULTS

A. Temperature dependence

In zero field, we study the temperature dependence of the magnetic excitations in BiCu₂PO₆ between 3 K and 20 K, well below the spin gap $\Delta/k_B \approx 34 \text{ K}$ [20]. Figure 2 presents the absorption spectra with the THz magnetic field $h\omega$ ap-

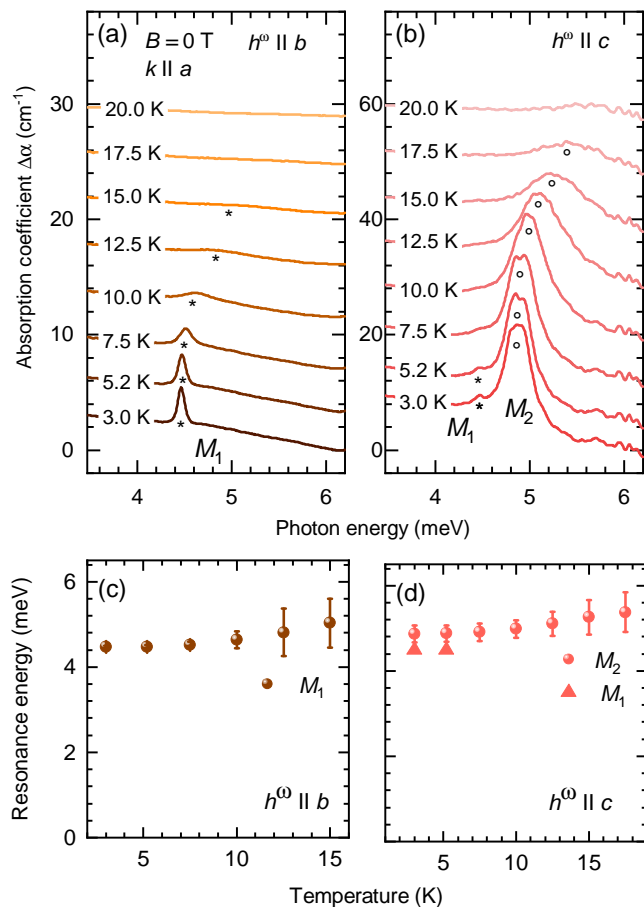


Figure 2. Temperature-dependent zero-field excitation spectra measured at 3 K in two polarizations, (a) $h^\omega \parallel b$ and (b) $h^\omega \parallel c$. (c) and (d) show the resonance energies extracted from the measurements shown in (a) and (b), respectively. The linewidth of the excitations is represented by the vertical bars.

plied along the crystallographic b axis [Fig. 2(a)], and along the c axis [Fig. 2(b)]. At the lowest temperature, two distinct modes emerge at 4.47 meV and 4.87 meV, as denoted by M_1 and M_2 , respectively. A polarization dependence is evidently observed. The M_1 mode exhibits a weaker absorption for $h^\omega \parallel c$ than for $h^\omega \parallel b$, whereas the M_2 mode is observed only for $h^\omega \parallel c$ with strong absorption. The temperature dependence of eigenfrequency and linewidth is summarized in Fig. 2(c)(d) for the corresponding polarizations. As the temperature increases, both modes display a thermally induced blueshift and broadening. Both effects can be explained by the thermal population and hardcore bosonic scattering of triplon modes [40–43].

The observed zero-field modes correspond to the energy of the low-lying excitations as resolved at $Q = (0, 0.5, 1)$ by INS spectroscopy [29]. Since the THz spectroscopy only probes the Γ -point, we attribute these modes to zone folding of the triplon branches, which could be due to the inequivalent next nearest neighbor interactions along the b axis [see Fig. 1(c)].

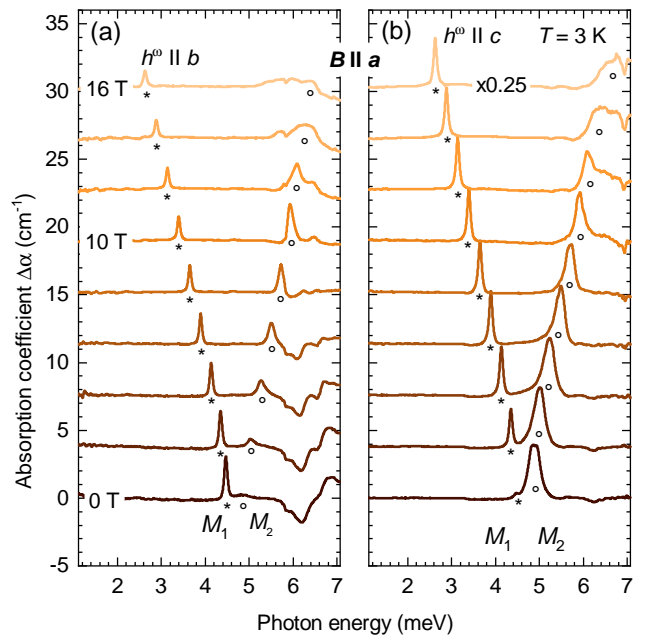


Figure 3. Magnetic excitations measured at 3 K in magnetic fields $B \leq 16$ T applied along the crystallographic a axis. Modes are indicated by asterisks (M_1) and circles (M_2). A constant vertical shift is applied for clarity. The panels show the different polarizations (a) $h^\omega \parallel b$ and (b) $h^\omega \parallel c$. In panel (b), the spectra are attenuated by a factor of 4 to have comparable peak heights in both panels.

B. Magnetic field dependence

Figure 3 presents the results for $B \parallel a$ in Faraday configuration. Due to the considerably higher absorption in $h^\omega \parallel c$ polarization, the intensity of spectra was multiplied by 0.25 in this polarization. We observe distinct behaviors for the two modes, M_1 and M_2 . With increasing field M_1 softens, while M_2 hardens. A polarization dependence is evident in the strength of the excitations. For $h^\omega \parallel b$, M_1 weakens and M_2 strengthens with the increase of B below 10 T. Conversely, for $h^\omega \parallel c$ the trend is reversed. At higher fields, M_2 broadens indicating a possible shift into a higher-energy phonon mode. No additional spin excitations were observed at higher energies due to strong absorption of phonon modes above 6.5 meV.

To study the spin dynamics when the field is tuned across the phase transition [37], we measured ESR transmission spectra of the sample in the same orientation in pulsed magnetic fields, which are presented in Fig. 4 for different frequencies from 96.0 to 144.5 GHz (corresponding to 0.4 meV–0.6 meV in photon energy). As indicated by the arrows, a field-dependent excitation is observed, whose energy increases linearly with increasing field strengths [see Fig. 8(a)]. However, this mode is detectable only within a narrow frequency range and emerges only above the critical field B_{c1} , which is characteristic for the field-induced phase. Although formation of a soliton lattice phase was suggested in a field-induced phase for $B \parallel b$ [34], our observed mode for $B \parallel a$ is

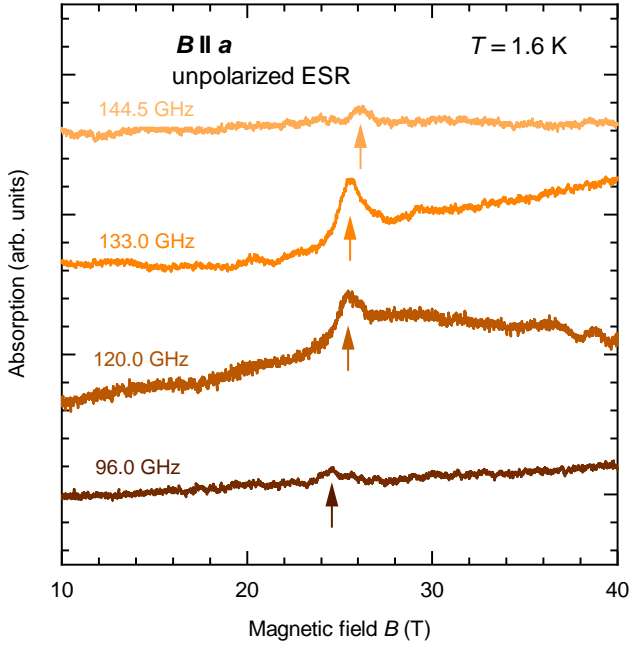


Figure 4. Unpolarized high-field ESR measurements performed in pulsed magnetic fields at 1.6 K. The absorption curves are shifted proportionally to the photon energy. Arrows point to the absorption peaks.

not necessarily related to soliton formation. This is not only because a soliton lattice may not be formed for $B \parallel a$ [37], but also because we cannot resolve the low-lying excitations in the high-field phase for $B \parallel b$.

Figure 5 presents the absorption spectra of the low-field measurements in Voigt geometry for $B \parallel b$. We observe also an evident polarization dependence. Whereas for $h^\omega \parallel b$ the excitation M_1 is more pronounced, M_2 is substantially enhanced for $h^\omega \parallel c$. We observe a strong field dependence for M_1 which is softening with increasing fields. The increase of its linewidth indicates a shorter lifetime approaching the critical field B_{c1} . M_2 is field-independent for $B \parallel b$ in clear contrast to its hardening behavior for $B \parallel a$. Since M_2 is magnetic field-independent in $h^\omega \parallel c$, the spectra are calculated from the measured $\Delta\alpha(B)$ using the 3 K zero field spectrum obtained from zero-field $\Delta\alpha(T)$ spectra.

To track the modes at higher fields and observe their characteristics at field-induced phase transitions, we performed measurements in static high magnetic fields. As shown in Fig. 6, only the field-dependent M_1 mode was detected, while the field-independent mode M_2 was not sensitively resolved by this experimental technique. At lower fields, the resonance energies of M_1 agree with the results in polarized spectroscopy. As the field increases, the softening of the mode becomes more pronounced. Approaching higher field strengths, the mode broadens and strengthens. Above the critical field at 24 T, the mode shifts continuously to lower energies while the softening weakens. At the same time, the linewidth decreases with increasing field. This indicates enhanced fluctuations at the critical field as is inline with approaching a continuous

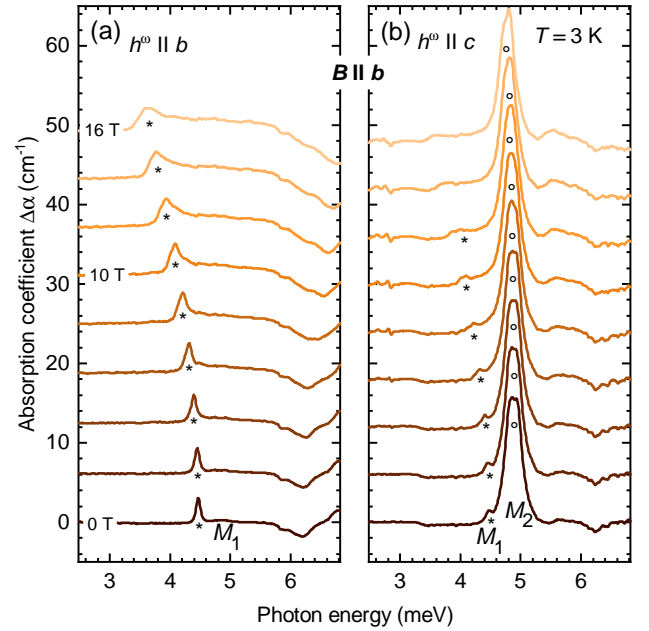


Figure 5. Magnetic excitations measured at 3 K in magnetic fields $B \leq 16$ T applied along the crystallographic b axis. Modes are indicated by asterisks (M_1) and circles (M_2). A constant vertical shift is applied for clarity. The panels show two different polarizations, (a) $h^\omega \parallel b$ and (b) $h^\omega \parallel c$.

quantum phase transition.

For fields applied along the c axis, i.e. within the ladder plane (see Fig. 1), the excitation spectra are presented in Fig. 7(a)(b) for two polarizations $h^\omega \parallel b$ and $h^\omega \parallel c$, respectively. At zero field the same two modes M_1 and M_2 are observed. However, their magnetic field dependence for this orientation is different in comparison to the other field orientations. While for $h^\omega \parallel b$ [Fig. 7(a)] the mode M_1 is more pronounced, we can see a stronger mode M_2 for $h^\omega \parallel c$ [Fig. 7(b)]. Moreover, another mode M_3 appears above 10 T. With increasing field the M_1 and M_2 modes soften slightly, whereas the M_3 frequency is nearly field-independent. The peak absorption of the modes varies in different magnetic fields. The M_1 mode becomes stronger with increasing magnetic field for both polarizations. For $h^\omega \parallel b$, the M_2 absorption increases first until 10 T and then decreases, while for $h^\omega \parallel c$ its intensity decreases monotonically with increasing field strengths. The intensity of the M_3 mode increases slightly with field.

We summarize all the observed spin excitations by plotting their eigenfrequencies as a function of magnetic field in Fig. 8 for three magnetic field orientations. For $B \parallel a$, we extrapolated the high-field data points of the M_1 mode by a linear fit, which yields a critical field of 36.6 T and $g \approx 2.20$ that is in good agreement with previous measurements [16]. The high-field ESR mode has a much lower energy (see also Fig. 4). A linear fit to its field dependence yields $g \approx 2.24$ and a critical field of $B_{c1} \approx 21.4$ T. This critical field B_{c1} corresponds to a field-induced phase transition because the spin gap closes. Its value is consistent with values obtained from specific heat

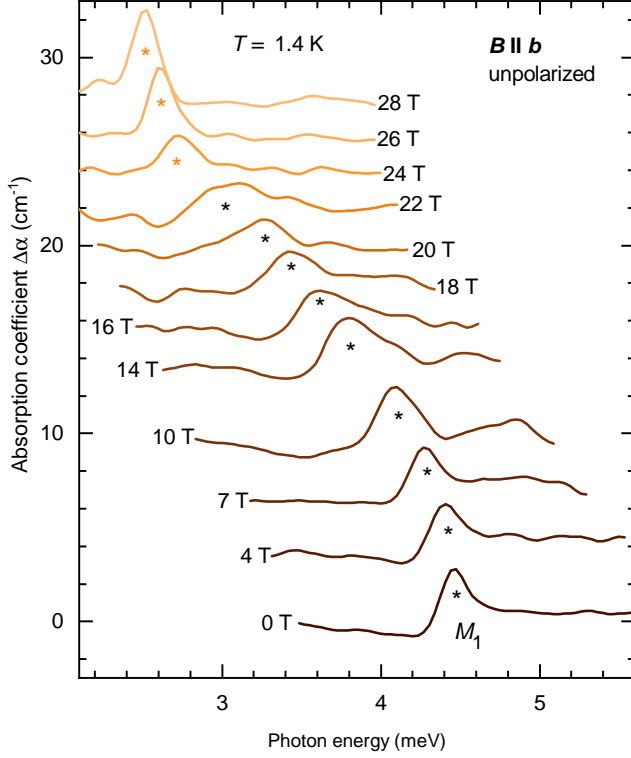


Figure 6. Unpolarized high-field FTIR measurements taken at 1.4 K with external magnetic fields $B \leq 28$ T applied along the crystallographic b axis. Asterisks indicate the excitation mode M_1 and their color changes above the critical field $B_{c1} \approx 22$ T. The spectra are shifted upwards proportional to the magnetic field strengths.

and magnetization measurements [16, 37]. Another interesting feature is the crossing of both extrapolations at $B \approx 29.0$ T which corresponds to a critical field for a field-induced first order phase transition [37]. For $B \parallel b$, M_2 exhibits a slight decrease with increasing field, while the softening of the M_1 mode is less pronounced in comparison to $B \parallel c$. M_1 can be followed in the unpolarized measurements even above the critical field $B_{c1} = 23$ T [37]. For $B \parallel c$, the field dependent softening of M_1 is even weaker, while the softening of the M_2 mode is more evident. M_3 , resolved above 12 T, is nearly independent on the field. Overall, the observed magnetic excitations clearly exhibit different field dependencies for different field orientations, which clearly indicates the presence of magnetic anisotropies. This can be ascribed to anisotropic g factors as well as bond-dependent DM interactions, which both will be modelled in detail in the next section.

IV. THEORETICAL ANALYSIS

In order to describe the magnetic dispersions theoretically, we set up an effective model in second quantization of the triplons. We employ the approach of continuous unitary transformations (CUT) as laid out generally in Refs. [44, 45] and specifically in Refs. [31, 33, 46]. Here, we outline the method

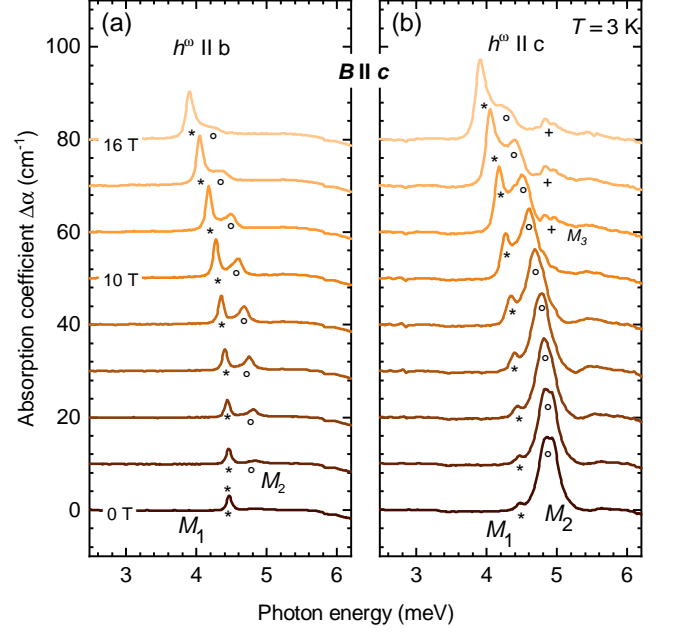


Figure 7. Magnetic excitations measured at 3 K in magnetic fields $B \leq 16$ T applied along the crystallographic c axis. Modes are indicated by asterisks (M_1), circles (M_2) and pluses (M_3). A constant vertical shift is applied for clarity. The panels show the different polarizations (a) $h\omega \parallel b$ and (b) $h\omega \parallel c$.

in broader strokes and refer the reader to the original work for more elaborate explanations.

Initially, the system is described by the Hamiltonian

$$\mathcal{H} = \mathcal{H}_{\text{ladder}} + \mathcal{H}_{\text{alter}} + \mathcal{H}_{\text{inter-ladder}} + \mathcal{H}_{\text{SOC}} + \mathcal{H}_{\text{magn}}, \quad (1a)$$

$$\mathcal{H}_{\text{ladder}}(J, x, y) = J \sum_{rd} \left[S_{rLd} S_{rRd} + x \sum_s S_{rsd} S_{r+1, sd} + xy \sum_s S_{rsd} S_{r+2, sd} \right], \quad (1b)$$

$$\mathcal{H}_{\text{alter}}(J, x, y, \delta) = Jxy\delta \sum_{rsd} (-1)^r S_{rsd} S_{r+2, sd}, \quad (1c)$$

$$\mathcal{H}_{\text{inter-ladder}}(J, \lambda) = \lambda J \sum_{rd} S_{rRd} S_{rL, d+1}, \quad (1d)$$

$$\mathcal{H}_{\text{SOC}}(\mathbf{D}, \Gamma) = \sum_{\langle rsd, r's'd' \rangle} \left[D_{rsd, r's'd'} (S_{rsd} \times S_{r's'd'}) + \sum_{\alpha\beta} \Gamma_{rsd, r's'd'}^{\alpha\beta} S_{rsd}^\alpha S_{r's'd'}^\beta \right], \quad (1e)$$

$$\mathcal{H}_{\text{magn}}(\mathbf{g}) = -\mu_B \sum_{\alpha} g^\alpha B^\alpha \sum_{rsd} S_{rsd}^\alpha. \quad (1f)$$

Figure 1 visualizes the interactions both in the three-dimensional crystal as well as in the two-dimensional theoretical model. Each vector operator S_{rsd} describes a spin on rung $r \in \mathbb{Z}$ and leg on the left or right-hand side $s \in \{L, R\}$ of the ladder $d \in \mathbb{Z}$, see Fig. 1(c). The Hamiltonian $\mathcal{H}_{\text{ladder}}$ describes an isotropic Heisenberg spin ladder with rung couplings J . The energy J sets the dominant energy scale. The

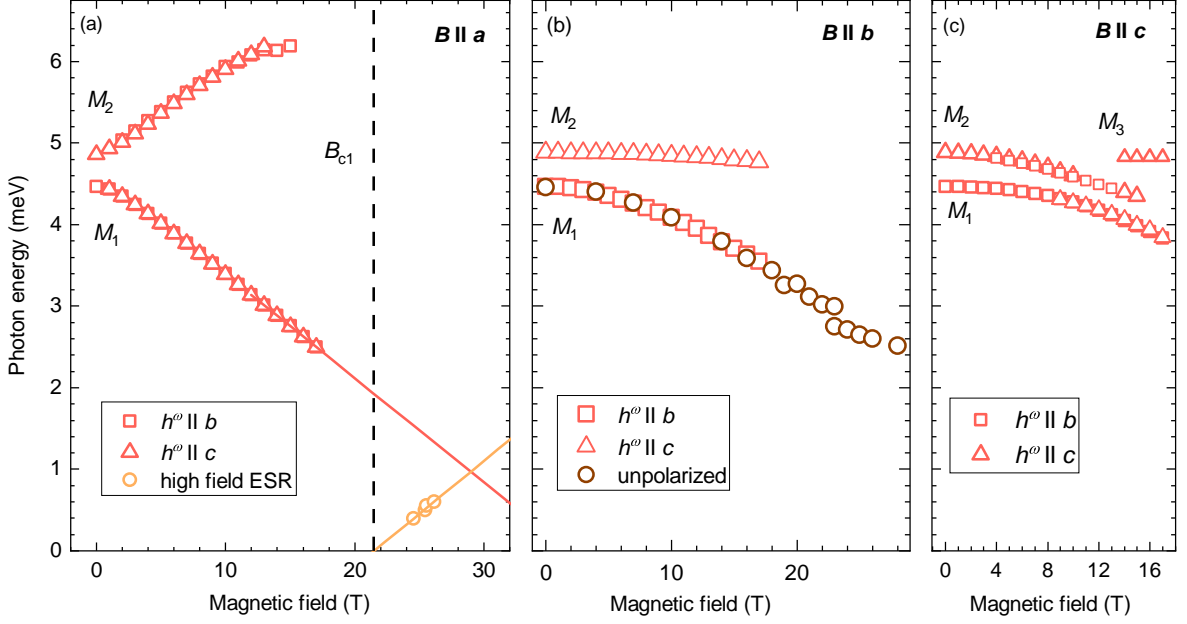


Figure 8. Field-dependent excitations. (a) Modes observed for external magnetic fields applied along the crystallographic a axis. Polarized low-field measurements (red) were supplemented by unpolarized high-field measurements in a pulsed magnet (yellow). (b) Magnetic excitations for magnetic fields applied along the b axis. Polarized low-field measurements (red) and unpolarized high-field measurements (brown) are shown. (c) Spin excitations measured for magnetic fields applied along the c axis in polarized low fields.

nearest-neighbor (NN) coupling along the legs has strength xJ and the next-nearest-neighbor (NNN) coupling along the legs has strength $xyJ(1 \pm \delta)$. So x describes the relative strength of the NN coupling on the legs to the rung coupling and y the relative strength of the NNN coupling to the NN coupling, both on the legs. The alternation $\pm xyJ\delta$ is described by $\mathcal{H}_{\text{alter}}$. The Heisenberg coupling of strength λJ between adjacent ladders is captured by $\mathcal{H}_{\text{inter-ladder}}$.

The Hamiltonian \mathcal{H}_{SOC} captures the effects of the relativistic spin-orbit coupling, implying the antisymmetric, anisotropic DM interactions \mathbf{D} and the symmetric anisotropic exchange Γ [47–49]. It has been shown that one should consider both the antisymmetric and symmetric anisotropic terms simultaneously [50]; in leading order they are linked by

$$\Gamma_n^{\alpha\beta} = \frac{D_n^\alpha D_n^\beta}{2J_n} - \frac{\delta_{\alpha\beta} \mathbf{D}_n^2}{6J_n} \quad (2)$$

with $\mathbf{D}_0 = (0, D_0^b, 0)$, $\mathbf{D}_1 = (D_1^a, D_1^b, D_1^c)$ and $\mathbf{D}_2 = (D_2^a, 0, D_2^c)$. The index n stands for the rung distance between the interaction partners, i.e., $J_0 = J$, $J_1 = xJ$, and $J_2 = xyJ$. Equation (2) ensures that the SAE does not comprise an isotropic contribution. Thus, we only fit the DM terms because SAE terms are then fixed as well.

The S_{rsd}^α are the components of \mathcal{S}_{rsd} with $\alpha \in \{a, b, c\}$. Finally, $\mathcal{H}_{\text{magn}}$ consists of the Zeeman energy with the magnetic field \mathbf{B} , Bohr magneton μ_B and the anisotropic \mathbf{g} tensors. The model parameters determining each term are indicated in brackets $\mathcal{H}(\cdot)$; they can be tuned for fitting to the experimental data.

The (approximate) diagonalization of Hamiltonian (1) is

done in the following steps:

1. using a CUT, an effective, bilinear model of the single ladder (1b) is computed in terms of the triplon operators. In parallel, the operator S_{rld}^c is also mapped to its leading expression in triplon language,
2. all other Hamiltonian terms are analytically expressed by the effective triplon operators from the previous step,
3. the eigenvalues are found via a Bogoliubov transformation, i.e., by numerically diagonalizing the commutation matrix of the Hamiltonian and the effective creation and annihilation operators.

A. Computing the Effective Single-Ladder Model

To obtain an effective model of the coupled spin ladders, it is convenient to start from the isotropic single-ladder model $\mathcal{H}_{\text{ladder}}(J, x, y)$ for $J, x, y \geq 0$ and reaching a description in terms of triplons by CUT. Note that the antiferromagnetic NN and NNN couplings lead to a frustrated system, i.e., frustration is present for $x, y > 0$. First, we describe the case of separated dimers ($x = y = 0$), for which the elementary excitations are completely local triplets, i.e., no distinction between local triplets and the more distributed triplons is necessary. The expansion in x at finite value y corresponds to an expansion in the range of the effective couplings leading to a gradual distribution of the triplons over more and more rungs: they become smeared out. This expansion is stable even for $x, y \gtrsim 1$, since

the triplons become distributed over more and more rungs, but still on a finite number of them. They do not delocalize completely [46, 51].

To express (1b) in triplon language, the spin operators are transformed into triplet operators \tilde{t}_{rd}^α of flavor $\alpha \in \{a, b, c\}$ at rung r on ladder d by substituting

$$2S_{rLd}^\alpha = +\tilde{t}_{rd}^\alpha + \tilde{t}_{rd}^{\alpha\dagger} - i \sum_{\beta\gamma} \epsilon_{\alpha\beta\gamma} \tilde{t}_{rd}^{\beta\dagger} \tilde{t}_{rd}^\gamma, \quad (3a)$$

$$2S_{rRd}^\alpha = -\tilde{t}_{rd}^\alpha - \tilde{t}_{rd}^{\alpha\dagger} - i \sum_{\beta\gamma} \epsilon_{\alpha\beta\gamma} \tilde{t}_{rd}^{\beta\dagger} \tilde{t}_{rd}^\gamma, \quad (3b)$$

similar to what is done with bond operators in Ref. [1]. Note that there can be either none or at most one triplet per rung so that these excitations are hardcore bosons.

The resulting triplet Hamiltonian is systematically mapped to an effective triplon model

$$\mathcal{H}_{\text{ladder}}^{\text{eff}}(J, x, y) = J \sum_{k\lambda} \omega_k(x, y) t_k^{\alpha\dagger} t_k^\alpha \quad (4)$$

with triplon operators t_k^α of flavor $\alpha \in \{a, b, c\}$ and momentum k in y -direction (the direction of the ladders) with single-triplon dispersion $\omega_k(x, y)$. This is achieved by CUTs, i.e., a controlled change of basis. In parallel, the single-spin operator in momentum space S_{ksd}^c is subjected to the same change of basis, yielding

$$S_{ksd}^{\alpha, \text{eff}}(x, y) = (-1)^s a_k(x, y) (t_{kd}^{\alpha\dagger} + t_{-k,d}^\alpha) + \dots \quad (5)$$

This representation is used to express all the parts of the full Hamiltonian (1) which do not belong to the isolated isotropic spin ladders. All terms in S_{ksd}^c which are nonlinear in the triplon creation and annihilation operators are indicated by the three dots in (5). Since the other parts of the Hamiltonian are small relative to the dominant couplings in the isolated isotropic spin ladder it is justified to neglect these nonlinear terms and to treat the triplons henceforth as standard bosonic operators, i.e., their hardcore property is neglected.

The basis change is performed using a CUT [51–53], specifically the deepCUT scheme [46] which includes infinite powers of x up to a certain range of interactions. Finally, all expressions are Fourier transformed in ladder direction b . In the deepCUT, both the Hamiltonian and the observable S_{rsd}^z are expanded in a growing basis of triplon operator monomials and a set of differential equations is set up which describe the the continuous basis change. The supplementary information of Ref. [51] describes the general CUT workflow for a spin ladder with $y = 0$ in more detail and Ref. [46] provides the specifics of the deepCUT scheme. Note that the deepCUT needs to be performed for a fixed parameter pair (x, y) and yields numerical values for $\omega_k(x, y)$ and $a_k(x, y)$.

The other terms in (1) are taken into account by using the transformed spin observable (5) and performing an additional Fourier transformation in c direction, i.e., perpendicular to the spin-ladder direction. This leads to a total momentum vector $\mathbf{k} = k\mathbf{e}_b + l\mathbf{e}_c = (k, l)$. The full effective Hamiltonian reads

$$\mathcal{H}^{\text{eff}} = \mathcal{H}_{\text{ladder}}^{\text{eff}} + \mathcal{H}_{\text{alter}}^{\text{eff}} + \mathcal{H}_{\text{inter-ladder}}^{\text{eff}} + \mathcal{H}_{\text{SOC}}^{\text{eff}} + \mathcal{H}_{\text{magn}}^{\text{eff}}, \quad (6a)$$

$$\mathcal{H}_{\text{ladder}}^{\text{eff}}(J) = J \sum_{k\alpha} \omega_k t_k^{\alpha\dagger} t_k^\alpha, \quad (6b)$$

$$\mathcal{H}_{\text{alter}}^{\text{eff}}(J, \delta) = 2Jxy\delta \sum_{k\alpha} a_k a_{k+\pi} \cos(2k) \left(t_k^{\alpha\dagger} t_{-k-(\pi,0)}^{\alpha\dagger} + 2t_k^{\alpha\dagger} t_{k+(\pi,0)}^\alpha + t_{k-k-(\pi,0)}^\alpha \right), \quad (6c)$$

$$\mathcal{H}_{\text{inter-ladder}}^{\text{eff}}(J, \lambda) = -\lambda J \sum_{k\alpha} a_k^2 \cos(2l) \left(t_k^{\alpha\dagger} + t_{-k}^\alpha \right) \left(t_k^\alpha + t_{-k}^{\alpha\dagger} \right), \quad (6d)$$

$$\mathcal{H}_{\text{magn}}^{\text{eff}}(\mathbf{g}) = -i\mu_B \sum_{\alpha} g^\alpha B^\alpha \sum_{k\beta\gamma} \epsilon_{\alpha\beta\gamma} t_k^{\beta\dagger} t_k^\gamma \quad (6e)$$

with effective DM and SAE interactions

$$\begin{aligned} \mathcal{H}_{\text{SOC}}^{\text{eff}}(D_0^b, D_1, D_2^c) = & + 4D_1^c i \sum_k a_k^2 \sin(k) \left[t_k^{\alpha\dagger} \left(t_{(-k,l)}^{b\dagger} + t_k^b \right) - \text{H.c.} \right] \\ & + 4D_2^c i \sum_k a_k a_{k+\pi} \sin(2k) \left[t_k^{\alpha\dagger} \left(t_{(-k-\pi,l)}^{b\dagger} + t_{(k+\pi,l)}^b \right) - \text{H.c.} \right] \\ & + \sum_{k\alpha} a_k^2 \left(2\Gamma_2^{\alpha\alpha} \cos(2k) + 2\Gamma_1^{\alpha\alpha} \cos(k) - \Gamma_0^{\alpha\alpha} \right) \left(t_k^{\alpha\dagger} t_{-k}^{\alpha\dagger} + 2t_k^{\alpha\dagger} t_k^\alpha + t_k^\alpha t_{-k}^\alpha \right) \\ & + 2 \sum_k a_k a_{k+\pi} \left[\left(\Gamma_1^{ba} e^{-ik} - \Gamma_1^{ab} e^{ik} \right) \left(t_{-k-(\pi,0)}^{b\dagger} + t_{k+(\pi,0)}^b \right) + \text{H.c.} \right]. \end{aligned} \quad (7)$$

Ref. [31] provides a full symmetry analysis for the DM and SAE terms.

All remaining model parameters in (6) and (7) that can be easily tuned are indicated in brackets $\mathcal{H}(\cdot)$. The parameters (x, y) are not listed explicitly, since changing them requires an additional deepCUT to obtain updated $\omega_k(x, y)$ and $a_k(x, y)$. We point out, however, that we tested multiple pairs (x, y) during fitting and chose the best result, which turned out to be at $(x, y) = (1.2, 0.85)$ in accordance with Refs. [31–33].

B. Diagonalization of the Full Effective Hamiltonian

The eigenenergies of the effective Hamiltonian (6a) are determined by a generalized Bogoliubov transformation [54]. This is possible if the triplons are considered as usual bosons without further constraints. This is justified if the non-diagonal terms to be taken into account by the Bogoliubov transformation are small relative to the diagonal ones. To find the appropriate transformation, the commutator

$$[\mathcal{H}, v] = w, \quad v = \sum_n v_n O_n, \quad w = \sum_n w_n O_n \quad (8)$$

is set up, where $\{O_n\}$ is a minimal set of basis operators such that the commutation equations are closed. Then the action of the commutation with the Hamiltonian can be described by a commutation or dynamic matrix \mathbf{M} [31, 55]

$$[\mathcal{H}, O_n] = \sum_m M_{nm} O_m \quad (9)$$

which allows one to compute the vectors of the coefficients according to

$$\mathbf{M}\mathbf{v} = \mathbf{w}. \quad (10)$$

The eigenenergies are found by diagonalizing the matrix \mathbf{M} . They appear in pairs $(\omega, -\omega)$ with $\omega > 0$ since we always include both, creation and annihilation operators. The eigenvectors provide further information about which operators contribute to which eigenmodes.

The minimal basis set for the full Hamiltonian is $\{O_n\} = \{t_k^{\alpha\uparrow}, t_{k+(\pi,0)}^{\alpha\uparrow}, t_{-k}^{\alpha}, t_{-k-(\pi,0)}^{\alpha}\}$ with $\alpha \in \{a, b, c\}$. For a given set of parameters (x, y, θ) with $\theta = (J, \lambda, D_0^b, \mathbf{D}_1, D_2^a, D_2^c, \mathbf{g}, \delta)$, a 12×12 matrix needs to be diagonalized for each data point (\mathbf{k}, \mathbf{B}) of interest, i.e., for each combination of momentum and magnetic field.

The full derivation of the matrix \mathbf{M} is explained in Refs. [31, 55]. We use

$$\mathbf{M}(\mathbf{k}, \mathbf{B}) = \begin{pmatrix} \mathbf{M}^{aa} & \mathbf{M}^{ab} & \mathbf{0}_{4 \times 4} \\ \mathbf{M}^{ba} & \mathbf{M}^{bb} & \mathbf{0}_{4 \times 4} \\ \mathbf{0}_{4 \times 4} & \mathbf{0}_{4 \times 4} & \mathbf{M}^{cc} \end{pmatrix} + \begin{pmatrix} \mathbf{0}_{4 \times 4} & \mathbf{H}^{ab} & \mathbf{H}^{ac} \\ \mathbf{H}^{ba} & \mathbf{0}_{4 \times 4} & \mathbf{H}^{bc} \\ \mathbf{H}^{ca} & \mathbf{H}^{cb} & \mathbf{0}_{4 \times 4} \end{pmatrix}, \quad (11a)$$

$$\mathbf{H}^{\alpha\beta} = -i\mu_B \mathbf{1}_{4 \times 4} \sum_{\alpha} \epsilon_{\alpha\beta\gamma} B^{\gamma} g^{\alpha}, \quad (11b)$$

$$\mathbf{M}^{\alpha\alpha} = \begin{pmatrix} \omega_k + A_k^{\alpha} & J_{2,k} & -A_k^{\alpha} & -J_{2,k} \\ J_{2,k} & \omega_{k+(\pi,0)} + A_{k+(\pi,0)}^{\alpha} & -J_{2,k} & -A_{k+(\pi,0)}^{\alpha} \\ A_k^{\alpha} & J_{2,k} & -\omega_k - A_k^{\alpha} & -J_{2,k} \\ J_{2,k} & A_{k+(\pi,0)}^{\alpha} & -J_{2,k} & -\omega_{k+(\pi,0)} - A_{k+(\pi,0)}^{\alpha} \end{pmatrix}, \quad (11c)$$

$$\mathbf{M}^{ab} = \begin{pmatrix} \mathbf{C}_k & \mathbf{C}_k \\ \mathbf{C}_k & \mathbf{C}_k \end{pmatrix}, \quad \mathbf{M}^{ba} = \begin{pmatrix} -\mathbf{C}_k^{\text{T}} & \mathbf{C}_k^{\text{T}} \\ \mathbf{C}_k^{\text{T}} & -\mathbf{C}_k^{\text{T}} \end{pmatrix}, \quad \mathbf{C}_k = \begin{pmatrix} i\mathbf{C}_k & i\mathbf{F}_k^{-+} \\ i\mathbf{F}_k^{++} & i\mathbf{C}_{k+\pi} \end{pmatrix}, \quad (11d)$$

with

$$A_{k,l}^{\alpha} = 2a_k^2 \left[-\lambda J \cos(2l) - \Gamma_0^{\alpha\alpha} + 2\Gamma_1^{\alpha\alpha} \cos(k) + 2\Gamma_2^{\alpha\alpha} \cos(2k) \right], \quad (12a)$$

$$J_{2,k} = 4Jxy\delta a_k a_{k+\pi} \cos(2k), \quad (12b)$$

$$\mathbf{C}_k = 4D_1^c a_k^2 \sin(k), \quad (12c)$$

$$\mathbf{F}_k^{\pm\pm} = 4a_k a_{k+\pi} \left(\pm \Gamma_1^{ab} \sin(k) \pm D_2^c \sin(2k) \right). \quad (12d)$$

Upon reproducing the derivation, we found different signs than in Ref. [31] in some terms in \mathbf{M}^{ab} and \mathbf{M}^{ba} . With the corrected signs the Bogoliubov transformation yields the pairwise opposite real eigenvalues as required. We find that the previous calculations underestimate the energy of the lowest

eigenmode. This has been corrected in our calculations.

We only consider magnetic fields parallel to one of the three directions $\{a, b, c\}$, so the submatrices $\mathbf{H}^{\alpha\beta}$ only mix the triplon operators with flavor of the two perpendicular directions. In particular, if the magnetic field points in c direction, the matrix is block-diagonal with a 4×4 c block and a 8×8 ab -block. In this case, the eigenvectors of the c block are completely independent from $B = |\mathbf{B}|$.

C. Results

The optimization yields several local minima of the cost function in the high-dimensional optimization space, for de-

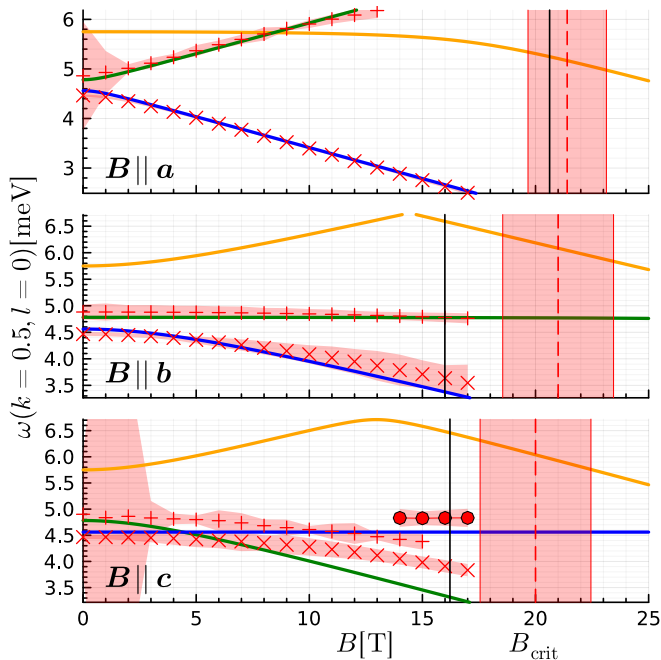


Figure 9. Results of minimizing the cost function (A1a). The three panels show the fit of the theoretical model energies (as blue, green and orange lines) to the experimental target data (red crosses with red ribbons indicating the region where the cost function increases by half a unit given the experimental uncertainties and the used weight factors, see also main text) for $\mathbf{B} \parallel \{a, b, c\}$, respectively. The vertical, red line indicates the target critical field with corresponding cost regime and the vertical, dashed, black line the theoretical critical field of the model where the spin gap closes.

tails see App. A where the cost function is defined. We present the best fits to the experimental data in Fig. 9. The fit parameters rounded to the leading digits are $(x, y) = (1.2, 0.85)$, $J = 9.524$ meV, $\lambda = 0.27$, $\delta = 0.095$, $\mathbf{g} = (2.167, 1.805, 2.0)$, $D_0^b = 0.46$, $\mathbf{D}_1 = (-0.05, -0.03, -0.02)$ and $(D_2^a, D_2^c) = (-0.06, -0.35)$. They were obtained in a minimization with cost parameters $(c_{M1}, c_{M2}, c_{M3, \mathbf{B} \parallel c}, c_{\text{gap}}, c_{\text{crit}}) = (1, 1, 10^4, 5 \cdot 10^3)$ and $c_{\text{crit}} = (2, 1, 1)$.

The colors for the modes are chosen blue, green and orange for the first, second and third smallest eigenenergies. For $\mathbf{B} \parallel a$, we observe that the second and third lowest mode typically cross. The algorithm has been implemented to consider this by reordering the eigenvalues such that the modes are kink-free.

The red ribbons visualize the experimental uncertainty, scaled such that when a mode or data point lies exactly at the edge of the corresponding ribbon, it adds 0.5 to the total cost. Therefore, it is a good indicator of how important each data point is for the fitting routine and of the relative uncertainties of the experimental mode data, but it should not be mistaken as the absolute experimental uncertainties. These ribbons also visualize why the weight factors c_{gap} and c_{crit} need to be so large: otherwise, the gap cost and critical cost would be insignificant for the optimization routine, i.e., the corresponding ribbons would be enormously wide.

The fitted modes shows quantitatively very good agreement

for $\mathbf{B} \parallel a$. For $\mathbf{B} \parallel b$ quantitative agreement within the experimental error bars can be achieved. The magnetically hard direction $\mathbf{B} \parallel c$ can capture the correct behavior for small magnetic fields but overestimates the down-bending of the lowest mode. Interestingly, our theoretical model seems to indicate that the mode M_3 (red circles) does not correspond to the third triplon mode, but further studies are called for clarification.

It is possible to find parameters yielding good fits for $\mathbf{B} \parallel c$ by strongly increasing the corresponding weight coefficients in the cost function. But this comes at the expense of significantly less convincing agreement of the other data points as well as critical fields.

The found DM interactions are quite large, in particular $D_0^b = 0.46$. It must be noted that since triplon-triplon interactions are not taken into account in the employed bilinear model, the fit parameters are effective DM interactions that are known to be larger than the ones when taking triplon interactions into account [29, 33]. The same applies to the g factors, which are in the range 1.8 – 2.2. They have to be interpreted as effective values within the bilinear model and may change due to renormalization effects if the triplon-triplon interaction is taken into account.

V. CONCLUSION

In summary, we document a comprehensive terahertz spectroscopy study of low-energy spin dynamics in a low-dimensional quantum magnet BiCu_2PO_6 at temperatures down to 1.4 K and in magnetic fields up to 60 T. For the magnetic fields applied in different crystallographic orientations, we observed evidently different field dependencies of the spin excitations. In particular, for field along the a axis, a field-induced phase transition at $B_{c1} = 21.4$ T is evidenced by the observation of a low-energy excitation above B_{c1} . The clear difference in the field-dependent evolution of the spin excitations indicates a strong magnetic anisotropy of the spin interactions.

To take into account the magnetic anisotropies theoretically, we introduce bond-dependent Dzyaloshinskii-Moriya interactions as well as the concomitant symmetric anisotropic exchanges and anisotropic g tensors in our model Hamiltonian, in addition to the Heisenberg exchange interactions between nearest- and next-nearest-neighbor spins. We performed a largely unbiased and automatic analysis of the magnetic dispersions in BiCu_2PO_6 on the level of a bilinear model with focus on the low-lying modes, by defining suitable cost functions that include the expected dispersion minimum and the critical magnetic field in a computationally efficient manner. With the determined fits, we observe very good agreement with the spectroscopic results in both the a and b field directions. While the low-field results in the c direction also align well, our analysis indicates that the theoretical model overestimates the downward bending of the lowest mode. Additionally, our model rules out the possibility of the high-field M_3 mode being the third triplon, raising questions about the physical origin of this mode.

From the theory side, it is desirable to investigate the spin

dynamics by an explicit inclusion of triplon-triplon interactions in the presence of magnetic fields. In zero field, calculations of this kind can be found in Refs. [29, 33]. From the experimental side, a comprehensive measurement of the spin excitations and possible excitation continua in magnetic fields by inelastic neutron scattering with energy and momentum resolution is highly interesting. For field applied along other directions than the b axis, a nuclear magnetic resonance measurement may reveal other features of field-induced phases than soliton lattice [28].

ACKNOWLEDGMENTS

We thank Y. Kohama for helpful discussions, and acknowledge support by the European Research Council (ERC) un-

der the Horizon 2020 research and innovation programme, Grant Agreement No. 950560 (DynaQuanta), by the Estonian Ministry of Education, personal research funding PRG736, and by the European Regional Development Fund project TK134 as well as by the Deutsche Forschungsgemeinschaft (German Science Foundation) in project UH90-14/1. The authors wish to thank the National Science and Technology Council for their support of this project under contract NSC111-2112-M-027-004-MY3. This work was supported by the Deutsche Forschungsgemeinschaft through the Würzburg-Dresden Cluster of Excellence on Complexity and Topology in Quantum Matter - *ct.qmat* (EXC 2147, project No. 390858490) and the SFB 1143, as well as by the HFML-RU/FOM and the HLD at HZDR, members of the European Magnetic Field Laboratory (EMFL).

-
- [1] S. Sachdev and R. N. Bhatt, *Phys. Rev. B* **41**, 9323 (1990).
 - [2] K. P. Schmidt and G. S. Uhrig, *Phys. Rev. Lett.* **90**, 227204 (2003).
 - [3] T. Giamarchi, C. Rüegg, and O. Tchernyshyov, *Nature Physics* **4**, 198 (2008).
 - [4] C. Rüegg, N. Cavadini, A. Furrer, H.-U. Güdel, K. Krämer, H. Mutka, A. Wildes, K. Habicht, and P. Vorderwisch, *Nature* **423**, 62 (2003).
 - [5] D. Yamamoto and I. Danshita, *Phys. Rev. B* **88**, 014419 (2013).
 - [6] T. Rice, *Science* **298**, 760 (2002).
 - [7] Y. H. Matsuda, N. Abe, S. Takeyama, H. Kageyama, P. Corboz, A. Honecker, S. R. Manmana, G. R. Foltin, K. P. Schmidt, and F. Mila, *Phys. Rev. Lett.* **111**, 137204 (2013).
 - [8] S. R. White, R. M. Noack, and D. J. Scalapino, *Phys. Rev. Lett.* **73**, 886 (1994).
 - [9] Z. Wang, M. Schmidt, Y. Goncharov, Y. Skourski, J. Wosnitza, H. Berger, H.-A. Krug von Nidda, A. Loidl, and J. Deisenhofer, *Journal of the Physical Society of Japan* **80**, 124707 (2011).
 - [10] Z. Wang, D. Kamenskyi, O. Cépas, M. Schmidt, D. L. Quintero-Castro, A. T. M. N. Islam, B. Lake, A. A. Aczel, H. A. Dabkowska, A. B. Dabkowski, G. M. Luke, Y. Wan, A. Loidl, M. Ozerov, J. Wosnitza, S. A. Zvyagin, and J. Deisenhofer, *Phys. Rev. B* **89**, 174406 (2014).
 - [11] D. C. Johnston, R. K. Kremer, M. Troyer, X. Wang, A. Klümper, S. L. Bud'ko, A. F. Panchula, and P. C. Canfield, *Phys. Rev. B* **61**, 9558 (2000).
 - [12] F. D. M. Haldane, *Phys. Rev. B* **25**, 4925 (1982).
 - [13] K. Okamoto and K. Nomura, *Physics Letters A* **169**, 433 (1992).
 - [14] Z. Wang, J. Wu, W. Yang, A. K. Bera, D. Kamenskyi, A. T. M. N. Islam, S. Xu, J. M. Law, B. Lake, C. Wu, and A. Loidl, *Nature* **554**, 219 (2018).
 - [15] Z. Wang, C.-M. Halati, J.-S. Bernier, A. Ponomaryov, D. I. Gorbunov, S. Niesen, O. Breunig, J. M. Klopff, S. Zvyagin, T. Lorenz, A. Loidl, and C. Kollath, *Nature* **631**, 760 (2024).
 - [16] A. A. Tsirlin, I. Rousochatzakis, D. Kasinathan, O. Janson, R. Nath, F. Weickert, C. Geibel, A. M. Läuchli, and H. Rosner, *Phys. Rev. B* **82**, 144426 (2010).
 - [17] M. Colmont, C. Darie, A. A. Tsirlin, A. Jesche, C. Colin, and O. Mentre, *Inorganic Chemistry* **57**, 6038 (2018).
 - [18] K. Hwang and Y. B. Kim, *Phys. Rev. B* **93**, 235130 (2016).
 - [19] B. Koteswararao, S. Salunke, A. V. Mahajan, I. Dasgupta, and J. Bobroff, *Phys. Rev. B* **76**, 052402 (2007).
 - [20] O. Mentré, E. Janod, P. Rabu, M. Hennon, F. Leclercq-Hugeux, J. Kang, C. Lee, M.-H. Whangbo, and S. Petit, *Phys. Rev. B* **80**, 180413(R) (2009).
 - [21] A. Antonakos, S. Wang, E. Liarokapis, and K. Conder, *Journal of Physics: Conference Series* **400**, 032004 (2012).
 - [22] T. Kawamata, H. Nagasawa, K. Naruse, M. Ohno, Y. Matsuoka, Y. Hagiya, M. Fujita, T. Sasaki, and Y. Koike, *Journal of the Physical Society of Japan* **87**, 074702 (2018).
 - [23] Y. Kohama, S. Wang, A. Uchida, K. Prsa, S. Zvyagin, Y. Skourski, R. D. McDonald, L. Balicas, H. M. Ronnow, C. Rüegg, and M. Jaime, *Phys. Rev. Lett.* **109**, 167204 (2012).
 - [24] O. Mentré, E. M. Ketatni, M. Colmont, M. Huve, F. Abraham, and V. Petricek, *Journal of the American Chemical Society* **128**, 10857 (2006).
 - [25] B. Koteswararao, A. Mahajan, L. Alexander, and J. Bobroff, *Journal of Physics: Condensed Matter* **22**, 035601 (2009).
 - [26] K.-Y. Choi, J. W. Hwang, P. Lemmens, D. Wulferding, G. J. Shu, and F. C. Chou, *Phys. Rev. Lett.* **110**, 117204 (2013).
 - [27] L. K. Alexander, J. Bobroff, A. V. Mahajan, B. Koteswararao, N. Laflorencie, and F. Alet, *Phys. Rev. B* **81**, 054438 (2010).
 - [28] F. Casola, T. Shiroka, S. Wang, K. Conder, E. Pomjakushina, J. Mesot, and H.-R. Ott, *Phys. Rev. Lett.* **105**, 067203 (2010).
 - [29] K. Plumb, K. Hwang, Y. Qiu, L. W. Harriger, G. Granroth, A. I. Kolesnikov, G. Shu, F. Chou, C. Rüegg, Y. B. Kim, *et al.*, *Nature Physics* **12**, 224 (2016).
 - [30] K. W. Plumb, Z. Yamani, M. Matsuda, G. J. Shu, B. Koteswararao, F. C. Chou, and Y.-J. Kim, *Phys. Rev. B* **88**, 024402 (2013).
 - [31] L. Splinter, N. A. Drescher, H. Krull, and G. S. Uhrig, *Phys. Rev. B* **94**, 155115 (2016).
 - [32] M. Malki, L. Müller, and G. S. Uhrig, *Phys. Rev. Res.* **1**, 033197 (2019).
 - [33] L. B. Müller and G. S. Uhrig, *Phys. Rev. B* **107**, L081102 (2023).
 - [34] F. Casola, T. Shiroka, A. Feiguin, S. Wang, M. S. Grbić, M. Horvatić, S. Krämer, S. Mukhopadhyay, K. Conder, C. Berthier, H.-R. Ott, H. M. Rønnow, C. Rüegg, and J. Mesot, *Phys. Rev. Lett.* **110**, 187201 (2013).
 - [35] M. Pikulski, T. Shiroka, F. Casola, A. P. Reyes, P. L. Kuhns, S. Wang, H.-R. Ott, and J. Mesot, *Scientific Reports* **10**, 15862

- (2020).
- [36] T. Sugimoto, M. Mori, T. Tohyama, and S. Maekawa, *Phys. Rev. B* **92**, 125114 (2015).
- [37] Y. Kohama, K. Mochizuki, T. Terashima, A. Miyata, A. Demuer, T. Klein, C. Marcenat, Z. L. Dun, H. Zhou, G. Li, L. Balicas, N. Abe, Y. H. Matsuda, S. Takeyama, A. Matsuo, and K. Kindo, *Phys. Rev. B* **90**, 060408(R) (2014).
- [38] I. Kézsmárki, D. Szaller, S. Bordács, V. Kocsis, Y. Tokunaga, Y. Taguchi, H. Murakawa, Y. Tokura, H. Engelkamp, T. Rößm, *et al.*, *Nature communications* **5**, 3203 (2014).
- [39] S. Zvyagin, J. Krzystek, P. van Loosdrecht, G. Dhahlenne, and A. Revcolevschi, *Physica B: Condensed Matter* **346-347**, 1 (2004).
- [40] B. Fauseweh, J. Stolze, and G. S. Uhrig, *Phys. Rev. B* **90**, 024428 (2014).
- [41] B. Fauseweh and G. S. Uhrig, *Phys. Rev. B* **92**, 214417 (2015).
- [42] E. S. Klyushina, A. C. Tiegel, B. Fauseweh, A. T. M. N. Islam, J. T. Park, B. Klemke, A. Honecker, G. S. Uhrig, S. R. Manmana, and B. Lake, *Phys. Rev. B* **93**, 241109(R) (2016).
- [43] B. Fauseweh and G. S. Uhrig, *Phys. Rev. B* **96**, 115150 (2017).
- [44] C. Knetter, K. P. Schmidt, M. Grüninger, and G. S. Uhrig, *Phys. Rev. Lett.* **87**, 167204 (2001).
- [45] C. Knetter, K. P. Schmidt, and G. S. Uhrig, *Journal of Physics A: Mathematical and General* **36**, 7889 (2003).
- [46] H. Krull, N. A. Drescher, and G. S. Uhrig, *Physical Review B* **86**, 125113 (2012).
- [47] I. Dzyaloshinsky, *Journal of Physics and Chemistry of Solids* **4**, 241 (1958).
- [48] T. Moriya, *Physical Review Letters* **4**, 228 (1960).
- [49] T. Moriya, *Physical Review* **120**, 91 (1960).
- [50] L. Shekhtman, O. Entin-Wohlman, and A. Aharony, *Phys. Rev. Lett.* **69**, 836 (1992).
- [51] G. Schmiedinghoff, L. Müller, U. Kumar, G. S. Uhrig, and B. Fauseweh, *Communications Physics* **5**, 10.1038/s42005-022-00986-0 (2022).
- [52] S. Kehrein, *The Flow Equation Approach to Many-Particle Systems* (Springer Berlin Heidelberg, 2006).
- [53] G. Schmiedinghoff and G. S. Uhrig, *SciPost Physics* **13**, 10.21468/scipostphys.13.6.122 (2022).

- [54] J.-P. Blaizot and G. Ripka, *Quantum theory of finite systems* (MIT Press, Cambridge, 1986).
- [55] L. B. Müller, *Quasiparticle decay induced by spin anisotropies in the frustrated spin ladder system BiCu₂PO₆* (TU Dortmund University, 442121 Dortmund, Germany, 2021).

Appendix A: Optimization of Model Parameters

We perform a numerical optimization to fit the model to the experimental data with as little bias as possible. First, we perform the CUT for a fixed pair of relative ladder couplings (x, y) . Ref. [31] analyzed which pairs (x, y) yield a reasonable dispersion and found a good approximation for $(x_0, y_0) = (1.2, 0.85)$. For our analysis, we performed computations with other pairs in the vicinity of (x_0, y_0) as well, but the pair $(1.2, 0.85)$ yields the best results. For any given pair (x, y) , the other parameters $\theta = (J, \lambda, D_0^b, \mathbf{D}_1, D_2^a, D_2^c, \mathbf{g}, \delta)$ are numerically optimized, using the diagonalization of the matrix $\mathbf{M}(\mathbf{k}, \mathbf{B})$ in order to compute the magnetic dispersions $\omega_{m_n}^\alpha(\mathbf{k}, B_n^\alpha)$, where $\alpha \in \{a, b, c\}$ denotes the direction of the magnetic field $\mathbf{B}_n \parallel \mathbf{e}_\alpha$. The index n stands for the concrete experimental data point for mode m_n and magnetic field B_n^α .

We optimize the parameters in such a way that they minimize a suitably chosen cost function in Eq. (A1). This cost function consists of several contributions. The term $C_{M1, M2}$ is the least-square sum of the deviations of the modes M_1 and M_2 ; similarly $C_{M3, B\parallel c}$ measures the deviations of the third mode if the magnetic field is applied along the c direction. The partial cost C_{gap} captures the deviation in the spin gap while C_{crit} assesses the deviation in the critical magnetic fields at which the valence bond phase breaks down. In total, we consider

$$C(\theta) = \frac{C_{M1, M2}(\theta) + C_{M3, H\parallel z}(\theta) + C_{\text{gap}}(\theta) + C_{\text{crit}}(\theta)}{C_{\text{all}}}, \quad (\text{A1a})$$

$$C_{M1, M2}(\theta) = \frac{c_{M1, M2}}{N_{M1, M2}} \sum_n \left| \frac{\omega_{m_n}^\alpha(\theta, \mathbf{k} = (\frac{\pi}{2}, 0), B_n^\alpha) - \omega_{m_n}^{\alpha, \text{target}}}{\Delta_n^\alpha} \right|^2, \quad (\text{A1b})$$

$$C_{M3, H\parallel z}(\theta) = c_{M3, B\parallel c} \left| \frac{\omega_{M3, B\parallel c}(\theta, \mathbf{k} = (\frac{\pi}{2}, 0), B_n^\alpha) - \omega_{M3, B\parallel c}^{\text{target}}}{\Delta_{M3}} \right|^2, \quad (\text{A1c})$$

$$C_{\text{gap}}(\theta) = c_{\text{gap}} \left(\left| \frac{k_{\text{gap}}(\theta) - k_{\text{gap}}^{\text{target}}}{k_{\text{gap}}^{\text{target}}} \right|^2 + \left| \frac{\omega_{\text{gap}}(\theta) - \omega_{\text{gap}}^{\text{target}}}{\omega_{\text{gap}}^{\text{target}}} \right|^2 \right), \quad (\text{A1d})$$

$$C_{\text{crit}}(\theta) = \frac{c_{\text{crit}}}{3} \sum_\alpha c_{\text{crit}}^\alpha \left| \omega_{\text{gap}}^\alpha(\theta, k_{\text{crit}}^\alpha, B_{\text{crit}}^{\alpha, \text{target}}) \right|^2 / \sum_\alpha c_{\text{crit}}^\alpha, \quad (\text{A1e})$$

$$k_{\text{crit}}^\alpha = \minarg_k \left(\left| \text{Re } \omega_{\text{gap}}^\alpha(\theta, k, B_{\text{crit}}^{\alpha, \text{target}}) \right| - \left| \text{Im } \omega_{\text{gap}}^\alpha(\theta, k, B_{\text{crit}}^{\alpha, \text{target}}) \right| \right), \quad (\text{A1f})$$

$$C_{\text{all}} = c_{M1, M2} + c_{M3, B\parallel c} + c_{\text{gap}} + c_{\text{crit}}. \quad (\text{A1g})$$

The coefficients (c_{M_1, M_2} , $c_{M_3, \mathbf{B} \parallel \mathbf{c}}$, c_{gap} , c_{crit}) are weight factors, which are tuned by hand in order to find good overall fits, and N_{M_1, M_2} is the number of sampling points of the dispersions used in the fit. The sampling points we use here are the terahertz spectroscopy results reported in this work. For the presented data, the weights were chosen to be (1, 1, 10^4 , $5 \cdot 10^3$) and $\mathbf{c}_{\text{crit}} = (2, 1, 1)$. Note that due to the differences in how the cost terms are computed, setting $c_{\text{gap}} = 10c_{M_1, M_2}$ does not mean that the error in the gap is 10 times more relevant for the optimization than other errors.

The M_3 mode for $\mathbf{B} \parallel \mathbf{c}$ is treated separately in $C_{M_3, \mathbf{B} \parallel \mathbf{c}}(\boldsymbol{\theta})$

instead of incorporating it in $C_{M_1, M_2}(\boldsymbol{\theta})$ because the experimental data suggests that it is a constant, flat mode. Therefore, we fit it only to the constant modes obtained from the 4×4 c block.

The experimental uncertainties Δ_n^α for the experimental data of the modes M_1 and M_2 are used to weight the fits according to the accuracy of the data. For the M_3 mode, the geometrically averaged Δ of all data points is used because the fitted mode is constant anyway.

The term $C_{\text{crit}}(\boldsymbol{\theta})$ quantifies the deviation in the critical magnetic field.